

DARK MATTER HALO PROFILES OF MASSIVE CLUSTERS: THEORY VERSUS OBSERVATIONS

SUMAN BHATTACHARYA^{1,2}, SALMAN HABIB^{1,2,3}, KATRIN HEITMANN^{1,2,3}, AND ALEXEY VIKHLININ^{4,5}

¹ High Energy Physics Division, Argonne National Laboratory, Argonne, IL 60439, USA

² Kavli Institute for Cosmological Physics, The University of Chicago, 5640 S. Ellis Avenue, Chicago, IL 60637, USA

³ Mathematics and Computer Science Division, Argonne National Laboratory, Argonne, IL 60439, USA

⁴ Harvard-Smithsonian Center for Astrophysics, 60 Garden Street, Cambridge, MA 02138, USA

⁵ Space Research Institute (IKI), Profsoyuznaya 84/32, Moscow 117997, Russia

Received 2012 October 3; accepted 2013 January 21; published 2013 March 5

ABSTRACT

Dark-matter-dominated cluster-scale halos act as an important cosmological probe and provide a key testing ground for structure formation theory. Focusing on their mass profiles, we have carried out (gravity-only) simulations of the concordance Λ CDM cosmology, covering a mass range of 2×10^{12} to $2 \times 10^{15} h^{-1} M_{\odot}$ and a redshift range of $z = 0-2$, while satisfying the associated requirements of resolution and statistical control. When fitting to the Navarro–Frenk–White profile, our concentration–mass (c – M) relation differs in normalization and shape in comparison to previous studies that have limited statistics in the upper end of the mass range. We show that the flattening of the c – M relation with redshift is naturally expressed if c is viewed as a function of the peak height parameter, ν . Unlike the c – M relation, the slope of the c – ν relation is effectively constant over the redshift range $z = 0-2$, while the amplitude varies by $\sim 30\%$ for massive clusters. This relation is, however, not universal: using a simulation suite covering the allowed w CDM parameter space, we show that the c – ν relation varies by about $\pm 20\%$ as cosmological parameters are varied. At fixed mass, the $c(M)$ distribution is well fit by a Gaussian with $\sigma_c/\langle c \rangle \simeq 1/3$, independent of the radius at which the concentration is defined, the halo dynamical state, and the underlying cosmology. We compare the Λ CDM predictions with observations of halo concentrations from strong lensing, weak lensing, galaxy kinematics, and X-ray data, finding good agreement for massive clusters ($M_{\text{vir}} > 4 \times 10^{14} h^{-1} M_{\odot}$), but with some disagreements at lower masses. Because of uncertainty in observational systematics and modeling of baryonic physics, the significance of these discrepancies remains unclear.

Key words: galaxies: clusters: general – galaxies: halos – methods: numerical

Online-only material: color figures

1. INTRODUCTION

According to the current cosmological model, structure forms in the universe primarily by the amplification of primordial fluctuations driven by the gravitational Jeans instability. The process of nonlinear structure formation is hierarchical and complex, the initial perturbations evolving eventually into a “cosmic web” network consisting of voids, filaments, and clumps. The clumps, called halos in cosmological parlance, are dark-matter-dominated localized mass overdensities with their own complex substructure. Observed baryonic systems such as galaxies and hot gas reside in these halos. Although the dark matter within halos cannot be observed directly, its presence can be inferred by dynamical arguments, and, much more directly, through gravitational lensing of background sources.

The notion of the dark-matter-dominated halo is one of the fundamental building blocks in studies of the formation of individual galaxies, galaxy groups, and galaxy clusters (for an overview, see Mo et al. 2010). The structure of halos has been extensively studied using N -body simulations over a wide range of halo masses. Even though individual halos can be and are dynamically and morphologically complex, it was shown by Navarro–Frenk–White (NFW; Navarro et al. 1996, 1997) that the spherically averaged density profiles of “relaxed” halos formed in cold dark matter (CDM) simulations can be described by a roughly universal functional form—the NFW profile—-independent of their mass, the spectrum of initial fluctuations, and cosmological parameters. The NFW profile has a fixed shape, albeit with two scale parameters; as applied to individual halos it has been remarkably successful and is often applied to all halos, regardless of their dynamical state. (When

applied to stacked or average halos, this profile is somewhat less successful, as discussed later below.)

The two parameters of the NFW profile are a mass and a scale radius. The scale radius, r_s , specifies the point where the logarithmic slope of the profile equals -2 (at small radii, the profile $\sim 1/r$, while at large radii, it asymptotes to $\sim 1/r^3$). Instead of r_s , one often uses the concentration, which is the radial scale set by the halo mass divided by r_s . In cluster cosmology, the usual key observable is the halo mass rather than the profile per se. The cluster mass function (cluster abundance, more generally) is a sensitive probe of dark energy, since clusters form very late during the epoch of dark energy dominance. However, measuring the concentration parameter, the simplest first measurement of a profile can also be very useful.

First, as shown originally by NFW, the concentration of a halo, c , has a strong correlation to its mass, M ; therefore measuring the c – M relation observationally is a direct test of the CDM paradigm. In fact, combining cluster c – M predictions and measurements and the measured gas mass fraction, one can aim to constrain Ω_m and σ_8 (Ettori et al. 2011). As another example, lensing shear peak counts, a proposed weak lensing survey cosmological probe, is very sensitive to the form of the c – M relation (King & Mead 2011). Finally, future measurements of the weak lensing power spectrum will probe small enough spatial scales that results will be sensitive to baryonic effects on the halo profile, i.e., modifications to the gravity-only c – M relation (White 2004; Zhan & Knox 2004). We will return to these points in more detail below.

The correlation of halo concentration with mass is based on the idea—as first explicated by NFW—that the concentration is determined by the mean density of the universe when the

halo is assembled, with higher concentrations corresponding to higher densities. Thus cluster mass halos, which are assembling today, should have a lower concentration than halos of lower mass that were built up at an earlier epoch, where the mean density was higher. Furthermore, one may expect this trend to flatten out (sufficiently) beyond the nonlinear mass scale M_* , and therefore, since M_* falls rapidly with redshift, flatten out over an extended range in mass as redshift increases. Although the general arguments are plausible and are broadly consistent with simulation results, a predictive theory for the mean of the c - M relation and its scatter does not exist. Several simple heuristic models tuned to simulations have been suggested (NFW; Bullock et al. 2001; Eke et al. 2001; Zhao et al. 2009), but their predictive status cannot be considered satisfactory, especially at the higher end of halo masses (see, e.g., Gao et al. 2008; Hayashi & White 2008; Macciò et al. 2008; Zhao et al. 2009). Indeed there is sufficient uncertainty even when comparing simulation results from different groups that the general problem is still open. However, as the mass resolution in large-volume simulations continues to improve, we may expect this situation to be merely temporary.

On the observational front, cluster (and group) halo profiles can be studied using both strong and weak gravitational lensing, individually and in combination (see, e.g., Comerford & Natarajan 2007; Broadhurst et al. 2008; Mandelbaum et al. 2008; Okabe et al. 2010; Oguri et al. 2012; Zitrin et al. 2011; Coe et al. 2012; Newman et al. 2012), projected gas density and temperature profiles from X-ray observations (see, e.g., Vikhlinin et al. 2006; Buote et al. 2007; Schmidt & Allen 2007; Gastaldello et al. 2007; Vikhlinin et al. 2009; Sun et al. 2009; Ettori et al. 2011), and galaxy kinematics (Diaferio et al. 2005; Rines & Diaferio 2006; Wojtak & Lokas 2010 and references therein). Results from these observations have generally shown qualitative agreement with the c - M relation obtained from simulations, although there have been difficulties with matching the shape and normalization. Additionally, there are discrepancies between different sets of observations, presumably because the underlying systematics are not fully understood and modeled.

The purpose of this paper is to present a set of predictions for the NFW mass profile targeted primarily toward massive clusters. To do so, however, a fairly large mass range must be considered in order to obtain a sufficiently well-defined c - M relation. Our simulations cover three orders of magnitude in mass ($\sim 10^{12}$ to $\sim 10^{15} h^{-1} M_\odot$) with very good control of statistics over the entire range. The high dynamic range and excellent statistics enable us to derive a new set of results for the mass profile, including profile evolution and probability distribution functions (PDFs) for the concentration as a function of mass. We compare our results with previous simulations and with a set of recent observations of the cluster mass profile.

This paper is organized as follows. In Section 2, we discuss general features of the c - M relation in the simulation context focusing on the role of differing definitions and analyses. In Section 3, we describe the main features of the simulation runs. We present our results for the c - M relation and its redshift evolution in Section 4. This is followed (Section 5) by a presentation of results from a suite of w CDM cosmologies in order to further study how the concentration depends on cosmology. Next, in Section 6, we provide a detailed comparison with recent observations, noting areas of agreement and disagreement. Finally, Section 7 is devoted to a summary of the results and further discussion. The Appendix discusses various systematic issues that need to be considered when deriving concentrations from

simulation results. A number of tests are used to illustrate these points and to verify the robustness of the numerical procedures carried out in this paper.

2. HALOS AND CONCENTRATIONS

Dark-matter-dominated halos are dynamically complicated and rendering them as simplified “few parameter” objects involves a fair degree of approximation, opening the possibility of biases in the sense that different procedures will inevitably yield different results—what these different results may imply for observations is yet another question. In this paper we adopt a minimal approach to describing halos; we consider the first approximate description of a halo to be a spherically averaged profile with a single power law and one overall parameter (e.g., singular isothermal sphere), and the NFW profile as essentially taking the next step with a broken power law and two parameters (the mass and the concentration). In three dimensions, halos are known to be triaxial with a major axis roughly twice as long as the two minor axes (roughly equal; Jing & Suto 2002). Spherical averaging of this profile yields the NFW broken power law.

In reality, halos have complicated substructures and complex infall regions, all of which may make interpreting the concentration somewhat nontrivial, as well as introduce projection-related biases in observations (e.g., White et al. 2010). Nevertheless, as shown by Evrard et al. (2008), cluster-scale systems with masses greater than $10^{14} h^{-1} M_\odot$ are dominated by large, primary halos—satellite halos carrying only $\sim 10\%$ of the mass—and possess a well-defined and regular virial relation. Therefore, it appears reasonable to proceed in the manner outlined above.

The lack of smoothness in the individual radial density profiles of halos—even at high mass resolution—means that the simple NFW description will have varying levels of success (see, e.g., Tormen et al. 1997; Lukić et al. 2009; Reed et al. 2011) on a halo-by-halo basis. Average or stacked profiles are of course much smoother; it turns out that such profiles systematically deviate from the NFW form and another scale parameter is often introduced to improve the fit, leading to the so-called Einasto profile (see, e.g., Gao et al. 2008). While this improves the stacked fit primarily at smaller radii, it has little effect on measurements of the concentration for individual halos (Gao et al. 2008; Reed et al. 2011). Since our primary objective is to carry out comparisons primarily against observations of individual objects rather than against correlation functions or stacked observations, we do not use the Einasto profile.

An important piece of missing physics in our simulations is the lack of non-gravitational baryonic effects. This is a very difficult problem to deal with for galaxy and group-scale objects, but less so for clusters. In clusters, the dominant form of atomic matter is not stars but hot gas. Gas cooling does not have a major effect on the profiles except close to the inner regions of the cluster, roughly $r < 0.1 R_{\text{vir}}$ (Kazantzidis et al. 2004; Duffy et al. 2010; Cui et al. 2012). Beyond this radius the gas distribution is determined by the self-consistent gravitational potential. Duffy et al. (2010) have carried out an extensive study of possible baryonic effects (cooling, feedback) on cluster profiles and concluded that the baryonic effects are likely to alter the concentration at most at the 10% level. This is roughly the level of systematic control over the current gravity-only measurements of halo concentrations, therefore we do not concern ourselves with estimating baryonic effects or trying to correct for them, beyond not fitting for the concentration at radii, $r < 0.1 R_{\text{vir}}$. The fact that we have good agreement with

observations for massive clusters (Section 6) may be viewed as added support to the argument that baryonic effects do not influence cluster profiles outside the inner regions; direct observational evidence for this can be found in Coe et al. (2012) and Newman et al. (2012; see also Mandelbaum et al. 2008).

A large number of numerical studies have been carried out investigating halo profiles and paying close attention to the behavior of the density cusp on the very smallest scales. We are, however, not concerned with these scales, but more with scales of the order of $\sim(0.1-1)R_{\text{vir}}$, since our target halos have relatively modest concentrations. Previous numerical simulations have found that in the region of interest to us the concentration is a slowly varying function of mass, typically described by power laws with index $\alpha \simeq -0.1$ at $z = 0$. These simulations have varied widely in dynamic range, box size, and mass resolution. Partly as a result of this, there have been some disagreement in the value of the slope and the normalization of the $c-M$ relation, and also some lack of clarity regarding the reasons underlying the differences.

Among the more recent studies are those involving the Millennium simulation (MS; Springel et al. 2005) with 2160^3 particles and a box of side $500 h^{-1}$ Mpc assuming a WMAP1 cosmology (Neto et al. 2007; Gao et al. 2008; Hayashi & White 2008). Halo profiles were investigated over a mass range of $10^{12}-10^{15} h^{-1} M_{\odot}$ and it was found that $\alpha \simeq -0.1$. These results were mostly in agreement with a simulation campaign conducted by Macciò et al. (2007, 2008) who covered a mass range $10^9-10^{13} h^{-1} M_{\odot}$, although with a slight discrepancy ($\sim 10\%$) in the normalization. Duffy et al. (2008) carried out another set of simulations with three different box sizes (25, 100, and $400 h^{-1}$ Mpc), each with 512^3 particles covering a mass range of $10^{11}-10^{15} h^{-1} M_{\odot}$ using the best-fit WMAP5 cosmology. They concluded that the median $c-M$ relation is lower by about 23% at the low-mass end and 16% at the high-mass end compared to the MS results in the mass range of $10^{11}-10^{14} h^{-1} M_{\odot}$. From yet another set of simulations, Klypin et al. (2011) and Prada et al. (2012) have claimed that the concentration, instead of flattening out at high mass, in fact rises.

Given this context, our primary purpose is to improve the statistical power in determining the $c-M$ relation and its scatter at high masses, while retaining good mass resolution, and second, to study the behavior as a function of redshift and cosmology. Finally, we note that the improved statistical power is important in comparing with observations of massive clusters as the numbers of well-observed clusters is expected to rise significantly in the near future (in the past, simulations may have contained only one cluster at the upper mass end, where we have hundreds).

3. SIMULATION SUITE

Throughout this paper, we use the following Λ CDM cosmology as a reference: $\omega_m = 0.1296$ ($\Omega_m = 0.25$), $\omega_b = 0.0224$ ($\Omega_b = 0.043$), $n_s = 0.97$, $\sigma_8 = 0.8$, and $h = 0.72$, where $\omega = \Omega h^2$ and Ω_m represents the total (dark + baryon) matter density. We assume spatial flatness. This model is in excellent agreement with the latest best-fit cosmological model provided by WMAP7 measurements (Komatsu et al. 2011). In order to cover a wide range of masses, we analyze three simulations with different volumes and number of particles. A summary of the runs is given in Table 1. The mass resolution in the large-box run is sufficient for measuring the concentrations for halo masses $> 10^{14} h^{-1} M_{\odot}$, with a minimum of 2000 particles per halo. At

Table 1
Description of the Simulation Suite

Code	Box (h^{-1} Mpc)	Softening (h^{-1} kpc)	Particles	m_p ($h^{-1} M_{\odot}$)
HACC (HACC)	2000	7	2048^3	6.5×10^{10}
HACC (HS)	512	7	2048^3	1.1×10^9
GADGET-2 (G)	936	36	1024^3	5.3×10^{10}
GADGET-2 (GS)	128	10	512^3	1.1×10^9

Note. Runs are referred to in the paper by the names in parentheses. HS was run up to $z = 2$.

$z = 0$, we have more than 100,000 such halos, therefore our statistical control may be considered to be more than satisfactory. In the MS and Duffy et al. (2008) simulations, the largest boxes used are of size $500 h^{-1}$ Mpc and $400 h^{-1}$ Mpc, respectively, with limited statistics for cluster size halos in the mass range $10^{14}-10^{15} h^{-1} M_{\odot}$. We provide a large sample of cluster size halos, with roughly 64 times more volume than in the MS run and 125 times more than in the simulations by Duffy et al. (2008).

The largest simulation (both with respect to volume and particle number) is carried out using our new Hardware/Hybrid Accelerated Cosmology Code (HACC) framework described in Habib et al. (2009) and Pope et al. (2010). This simulation covers a volume of $(2 h^{-1} \text{G pc})^3$ and evolves 2048^3 particles and was run on the hybrid supercomputer Cerrillos at Los Alamos National Laboratory. (Another 2048^3 particle run with a $512 h^{-1}$ Mpc box was used to test the results obtained at $z = 2$ from the GADGET-2 run described below.) The HACC framework has been designed with flexibility as a prime requirement; it is meant to be easily portable between high-performance computing platforms based on different architectures. The first version of the code has been optimized to run on the Cell-hybrid architecture shared by Roadrunner (the first computer to break the Petaflop barrier) and Cerrillos. An extension of this version of the code has been developed for hybrid CPU/GPU systems, written in OpenCL.

HACC's code structure is split into two components: a long-range force solver and a short-range module. The long-range force solver uses a parallel Particle-Mesh (PM) algorithm with spectral filtering and super-Lanczos differentiation (Hamming 1998). In this part of the code, the long-range force is calculated by depositing tracer particles onto a regular grid and using Fourier transform methods to solve the Poisson equation (with in effect a modified Green function) and then interpolating the force from the grid back onto the particles. The spectral component of the code is implemented in C++/MPI and can run on any standard parallel machine. The current two-dimensional domain-decomposed implementation of the fast Fourier transform allows it scale to millions of MPI ranks. The implementation of the particle deposition and force interpolation routines depends on the machine architecture. On Roadrunner and Cerrillos, these routines were implemented on the Cell processor.

The short-range module adds the high-resolution force between particles and can be implemented in different ways and on different platforms. On Cell and GPU-based systems, an N^2 -algorithm is used to evaluate the short-range forces (in chaining mesh patches), leading to a P³M implementation. This works well on hardware-accelerated machines since it is computationally intensive and uses a simple data structure. The P³M version of HACC has been extensively tested against

the code comparison suite results of Heitmann et al. (2005). On non-heterogeneous systems, such as the IBM BG/Q, the N^2 algorithm is replaced by a recursive coordinate bisection (RCB) tree method to guarantee good performance (Habib et al. 2012).

In addition to the main code base, a parallel analysis framework for HACC has been developed. This framework runs on conventional supercomputing hardware (or on the “top” layer of a heterogeneous system). Among other utilities, it contains a halo and subhalo finder. The halo finder was part of a recent comparison project (Knebe et al. 2011) and is used for the analysis results presented in this paper. Major parts of the HACC analysis framework have been implemented into ParaView and publicly released (Woodring et al. 2011).

The smaller simulations are carried out with GADGET-2, a publicly available TreePM code (Springel 2005). Of these, the larger simulation—(936 h^{-1} Mpc)³ volume, 1024³ particles—is part of the Coyote universe simulation suite (Heitmann et al. 2010, 2009; Lawrence et al. 2010) which spans 38 Λ CDM cosmologies. This simulation was also used to derive a high-precision Λ CDM mass function prediction (Bhattacharya et al. 2011). (The HACC mass function in the large-volume run presented here is in excellent agreement with these results.) The smallest of the three simulations—(128 h^{-1} Mpc)³ volume, 512³ particles—serves three purposes: (1) it allows us to probe halos at small masses, (2) it provides large overlap with previous work and therefore connects our new results to a mass range that has been extensively studied in the past, and (3) because it is run with a completely different code, it provides an excellent check on possible code-related systematics (for which we find no evidence; more details are in the Appendix).

The initial conditions for all three simulations are generated using transfer functions from the Code for Anisotropies in the Microwave Background (CAMB⁶; Lewis et al. 2000) and the Zel’dovich approximation at a high starting redshift, $z_i \simeq 200$. Further discussions regarding simulation accuracy issues can be found in the Appendix.

4. Λ CDM RESULTS

4.1. c - M Relation

In our simulations, we identify halos using a fast parallel friends-of-friends (FOF) finder (Woodring et al. 2011) with linking length $b = 0.2$. (The Appendix contains a discussion of how this choice can affect results.) The effects of major substructures, relevant for roughly a quarter of the halos (e.g., Lukić et al. 2009), are checked by using morphological cuts mentioned below. Since we are concerned only with the mass profiles and not the dynamical state of the halo, we do not use any velocity information (for instance, whether or not to unbind particles). Once a halo is found, we define its center via a density maximum criteria—the location of the particle with the maximum number of neighbors. This definition of the halo center is very close to that given by the potential minima. Given a halo center, we grow spheres around it and compute the mass in radial bins. Note that even though an FOF finder is used, the actual halo mass is defined by a spherical overdensity method, consistent with the approach followed in observations. (For discussions on halo mass, see White 2001; Lukić et al. 2009; More et al. 2011.) Although the mass could be measured independently of the concentration we fit both together to the

halo profile, as this is potentially less sensitive to fitting bias. (In practice, it makes little difference.)

We write the NFW profile as

$$\rho(r) = \frac{\delta \rho_{\text{crit}}}{(r/r_s)(1+r/r_s)^2}, \quad (1)$$

where δ is a characteristic dimensionless density and r_s is the scale radius of the NFW profile. The concentration of a halo is defined as $c_\Delta = r_\Delta/r_s$, where Δ is the overdensity with respect to the critical density of the universe, $\rho_{\text{crit}} = 3H^2/8\pi G$, and r_Δ is the radius at which the enclosed mass, M_Δ , equals the volume of the sphere times the density $\Delta\rho_{\text{crit}}$. We compute concentrations at two radii corresponding to $\Delta = 200$ and $\Delta = \Delta_{\text{vir}}$, corresponding in turn to $c_{200} = R_{200}/r_s$ and $c_{\text{vir}} = R_{\text{vir}}/r_s$. The value of Δ_{vir} is given by the spherical top-hat collapse model; it changes with redshift and cosmology and, for Λ CDM, can be approximated by a fitting formula $\Delta_{\text{vir}} = 18\pi^2 + 82x - 39x^2$ with $x = \Omega_m(z) - 1$, $\Omega_m(z) = \Omega_m(1+z)^3/(\Omega_m(1+z)^3 + \Omega_\Lambda)$ (Bryan & Norman 1998). For our reference cosmology, Δ_{vir} varies from ~ 95 to 170 over the range $z = 0-2$. We also provide a fit for the overdensity of 200 times the mean density, ρ_b , of the universe at a particular redshift, z . Written in terms of the critical density, this corresponds to $\Delta = 200\Omega_m(z)$ which varies from 50 to 180, over the range $z = 0-2$ for our reference cosmology.

The mass enclosed within a radius r for an NFW halo profile is given by

$$M(<r) = \frac{m(c_\Delta r/r_\Delta)}{m(c_\Delta)} M_\Delta, \quad (2)$$

where $m(y) = \ln(1+y) - y/(1+y)$. The mass in a radial bin is then

$$M_i = M(<r_i) - M(<r_{i-1}). \quad (3)$$

We fit Equation (3) to the mass contained in the radial bins of each halo, by minimizing the associated value of χ^2 as

$$\chi^2 = \sum_i \frac{(M_i^{\text{sim}} - M_i)^2}{(M_i^{\text{sim}})^2/n_i}, \quad (4)$$

where the sum is over the radial bins, n_i is the number of particles in a radial bin, M_i^{sim} is the mass in bin i calculated from the simulations, and M_i is the mass calculated assuming the NFW profile; 20 bins were used in the individual profile fits. The advantage of fitting mass in radial bins rather than the density is that the bin center does not have to be specified. Note that we explicitly account for the finite number of particles in a bin. This leads to a slightly larger error in the profile fitting but minimizes any possible bias due to the finite number of particles, especially near the halo center. More details about the fitting procedure are provided in the Appendix.

We fit for two parameters—the normalization of the profile and the concentration. Halo profiles are fitted in the radial range of approximately $(0.1-1)R_{\text{vir}}$. This choice is motivated partly by the observations of concentrations that typically exclude the central region of clusters (e.g., observations by Oguri et al. 2012 to which we compare our results in Section 6). More significantly, however, this excludes the central core which is sensitive to the effects of baryonic physics and numerical errors arising from limitations in both mass and force resolution, as discussed in the Appendix. As already mentioned, Duffy et al. (2010) have shown that, at $r < 0.1 R_{\text{vir}}$, halo profiles are sensitive to the impact of baryons with the profiles being affected at $r = 0.05 R_{\text{vir}}$ by as much as a factor of two.

⁶ <http://camb.info>

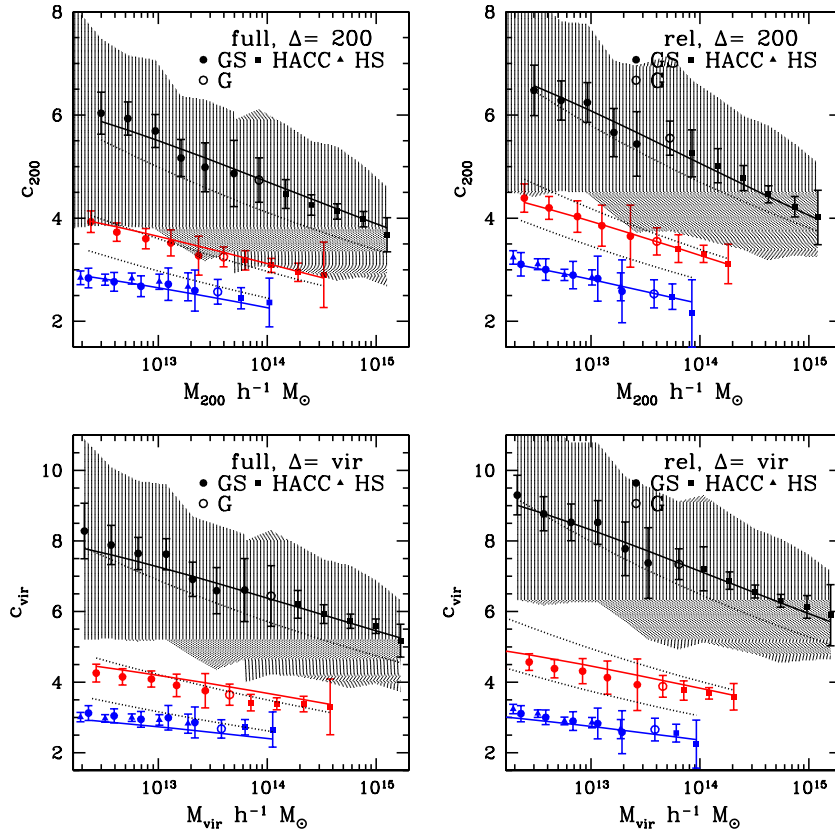


Figure 1. c - M relations at radii $r = R_{200}$ and $r = R_{\text{vir}}$ for $z = 0$ (black), 1 (red), and 2 (blue) for the full (left panels) and relaxed samples (right panels), combining results of multiple simulations. The black solid lines at $z = 0$ are power-law fits, $\alpha = -0.08$ for the full sample, and $\alpha = -0.084$ for the relaxed halos. The solid red and blue curves are from the global fit (across all redshifts) discussed in Section 4.2 and shown in Figure 2. The error bars represent the error in determining the mean of the concentration in each mass bin (the difference between the mean and the median is insignificant). At a given mass, the distribution of concentrations is Gaussian with standard deviation $\sigma_c/c \sim 1/3$ (cf. Section 4.3)—the shaded region shows the 1σ boundary for $z = 0$. The dotted curves are fitting formulae for the median concentration as given by Duffy et al. (2008).

(A color version of this figure is available in the online journal.)

In the Appendix we discuss the robustness of the obtained c - M relation as the fitting range is varied; we find that different fitting ranges—chosen with a fair degree of latitude—agree with each other to better than 10% accuracy (Figure 11).

The c - M relation is calculated by weighing the individual concentrations by the halo mass,

$$c(M) = \frac{\sum_i c_i M_i}{\sum_i M_i}, \quad (5)$$

where the sum is over the number, N_i , of the halos in a mass bin. The mass of the bin is given by

$$M = \sum_i M_i / N_i. \quad (6)$$

The error on $c(M)$ is the mass-weighted error on the individual fits plus the Poisson error due to the finite number of halos in an individual bin added in quadrature,

$$\Delta c(M) = \sqrt{\left(\frac{\sum_i \Delta c_i M_i}{\sum_i M_i}\right)^2 + \frac{c^2(M)}{N_i}}, \quad (7)$$

where Δc_i is the individual concentration error for each halo. The first term dominates toward the lower mass end where the individual halos have smaller number of particles and the

second term dominates toward the higher mass end, where there are fewer halos to average over.

Figure 1 shows the mean c - M relation obtained from our simulation runs weighted by the mass (Equation (5)). We show the c - M relation both for relaxed halos and for the full (relaxed + non-relaxed) sample.

To select the relaxed sample we use criteria similar to those of Neto et al. (2007) and Duffy et al. (2008), defining relaxed halos as those in which the difference between the location of the center of mass and the center density maximum is $< 0.07 R_{\text{vir}}$ (see also Thomas et al. 2001). Neto et al. (2007) have used two additional criteria to select their relaxed sample but found that the difference in the center of halos method already selected most of the relaxed sample. We do not impose their additional criteria as it would lead to insignificant changes in our sample selection. At $z = 0$, the relaxed fraction varies from 0.73 to 0.6 for $M_{200} = 10^{12}$ – $7.5 \times 10^{14} h^{-1} M_\odot$, and the results for this fraction are consistent with those found by Neto et al. (2007). As the redshift increases, one would expect this ratio to decrease as a function of mass. For the bins centered at $M_{200} = 2.47 \times 10^{12} h^{-1} M_\odot$, and $M_{200} = 1.39 \times 10^{13} h^{-1} M_\odot$, the values are 0.77, 0.69, 0.67, and 0.74, 0.63, 0.63, at $z = 0, 1, 2$, respectively. At $M_{200} = 1.39 \times 10^{14} h^{-1} M_\odot$, the values are 0.63, 0.48, at $z = 0, 1$ (insufficient statistics at $z = 2$).

From Figure 1 it is clear that the c - M relation becomes considerably flatter at $z > 0$, with the full sample relation flattening more at higher redshift compared to that for the

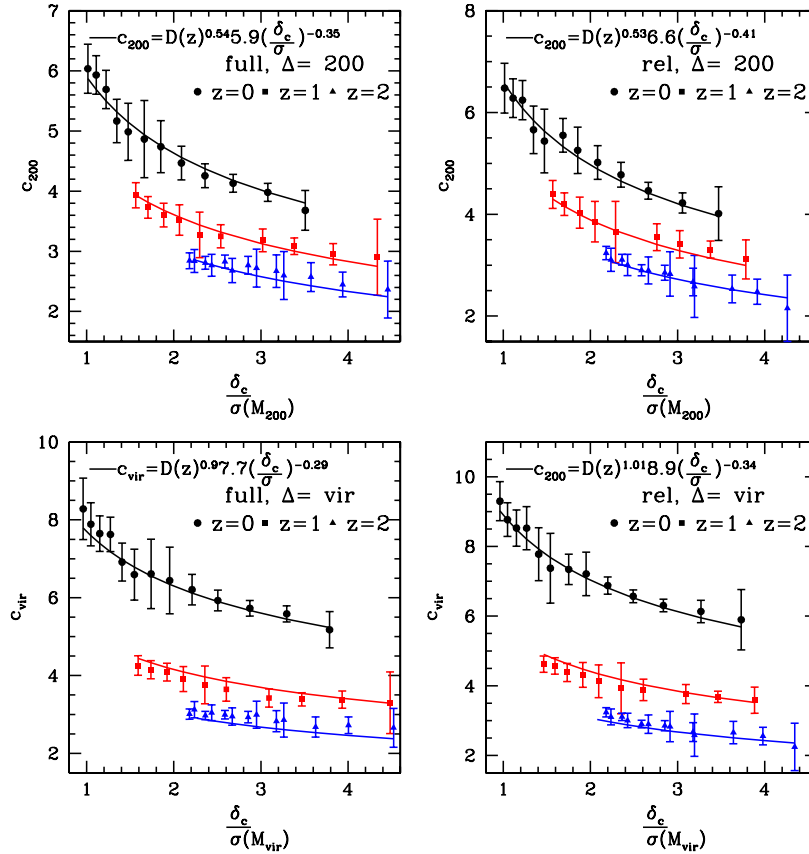


Figure 2. c - ν relations at radii $r = R_{200}$ and $r = R_{\text{vir}}$ for $z = 0, 1, 2$, for the relaxed and full samples where $\nu = \delta_c / \sigma(M_\Delta)$ with $\delta \sim 1.676$, varying only mildly with redshift. The lines are global fits to the data points using a simple assumption for redshift evolution.

(A color version of this figure is available in the online journal.)

relaxed sample. The c - M relation for the relaxed sample has on an average a 10% higher amplitude compared to that for the full sample. The c - M relation at the radius corresponding to $\Delta = \Delta_{\text{vir}}$ has about a 30% higher amplitude compared to that at $\Delta = 200$.

Because the cosmologies considered are essentially the same, we can directly compare our results with those of Duffy et al. (2008), although their statistics become somewhat limited near the upper end of halo masses. We find that at $z = 0$, at cluster mass scales, their c - M amplitude is about 15% lower compared to our results. At $z = 2$, the results from Duffy et al. (2008) are about 15% higher, but with significant scatter. In general, their redshift evolution appears to be slightly compressed, more so in the case of relaxed halos. But given the statistical limitations already mentioned (cf. Figure 2 of Duffy et al. 2008), we may consider the comparison to be quite reasonable. Another reason for not expecting an exact match is that the fitting range we use and the one in Duffy et al. (2008) are different, being $0.1 R_{\text{vir}}$ and $0.05 R_{\text{vir}}$, respectively. As seen in Figure 11, a larger value of the minimum fit radius tends to increase the concentration.

At $z = 0$, our results can be fitted very accurately by a power law with the exponent, $\alpha = -0.08$ and -0.084 for the full and the relaxed sample. The logarithmic slope corresponding to the full sample is precisely that found by Hayashi & White (2008) using the halo-density cross-correlation applied to data from the MS. The normalization, however, is not expected to be the same because of the high value of $\sigma_8 = 0.9$ chosen for the MS. Note that three different analyses of the MS (and an associated smaller volume, higher mass resolution run) have produced slightly discrepant results, differing from each other at

the 10%–20% level (Neto et al. 2007; Gao et al. 2008; Hayashi & White 2008). This is probably a useful empirical measure of the systematic issues inherent to halo selection and fitting. In general, the MS results are consistently higher at all redshifts by about 15% at $z = 0$ to about 30% at $z = 2$ largely because of the higher value of σ_8 .

4.2. The c - ν Relation

We find that the c - M relation becomes almost flat at higher redshift, with $c_{200} \sim 3$ in a way similar to the findings of Gao et al. (2008; although for a higher σ_8 in their case). Gao et al. (2008) use the Einasto profile for stacked halos—alternatively, we ask if it is possible to explain the flattening of the c - M relation with redshift using only the NFW profile. To do this, we follow the strategy adopted in parameterizing halo mass functions and investigate the concentration measurements as a function of the rms density fluctuation $\sigma(M, z)$ rather than M (for each of the three halo mass definitions). As the central variable, we use the peak height parameter, $\nu = \delta_c(z) / \sigma(M, z)$, where $\delta_c(z)$ is the linear collapse threshold. ($\delta_c = 1.673$ for the reference cosmology and varies only mildly with cosmology and redshift.) $\sigma(M, z)$ specifies the variance of the matter fluctuations over the scale $\propto M^{1/3}$ at a redshift z . As shown in Figure 2, the shape of the c - ν relation is approximately constant over the redshift range $z = 0$ – 2 , in contrast to the shape of the c - M relation.

Overall, the evolution of $c_{200}(\nu)$ proceeds as $\sim D(z)^{0.5}$ where $D(z)$ is the linear growth factor at redshift z , or by about 30% from $z = 0$ to 2. The overall z -evolution in our work is roughly

Table 2
 $c(\nu)$ - ν Fitting Formulae

	$\Delta = 200$	$\Delta = \Delta_{\text{vir}}$	$\Delta = 200\rho_b$
Full	$D(z)^{0.54} 5.9\nu^{-0.35}$	$D(z)^{0.9} 7.7\nu^{-0.29}$	$D(z)^{1.15} 9.0\nu^{-0.29}$
Relaxed	$D(z)^{0.53} 6.6\nu^{-0.41}$	$D(z)^{1.01} 8.9\nu^{-0.34}$	$D(z)^{1.2} 10.1\nu^{-0.34}$
Std. Dev.	$\sigma_c = 0.33c_\Delta$		
ν - M	$\nu(M, z) \approx \frac{1}{D(z)} \left[1.12 \left(\frac{M}{5 \times 10^{13} h^{-1} M_\odot} \right)^{0.3} + 0.53 \right]$		

consistent with the z -evolution seen in the MS result of Gao et al. (2008). The evolution of $c_{\text{vir}}(\nu)$ possesses a somewhat larger dynamic range and the evolution goes as $\sim D(z)$. The slope of the c - ν relation is slightly larger for $\Delta = 200$ compared to that for $\Delta = \Delta_{\text{vir}}$. The amplitude of the c - ν relation is only a little larger for the relaxed sample compared to the full sample (by about $\sim 10\%$).

Fitting formulae for $c(\nu)$ as derived from the simulations for the reference Λ CDM cosmology are given in Table 2. We also provide an approximate fitting formula relating ν and M valid for all overdensities, redshift, and cosmology, which can then be used to convert the relations for c - ν to those for c - M . Table 2 also provides the c - ν relation for $\Delta = 200\Omega_m(z)$ corresponding to an overdensity of $200\rho_b$. At $z = 0$, for the reference cosmology used here, $200\rho_b$ is about half of the virial overdensity. Consequently, the c - ν amplitude is about 30% higher compared to the amplitude at the virial density. At $z = 1$ and 2, the mean density and the virial density become comparable. Thus, the c - ν relation for $\Delta = 200\Omega_m(z)$ has more z -evolution when compared to that for the virial density.

4.3. The Distribution of Concentrations

The mean c - M relation needs to be augmented with a good quantitative understanding of the concentration scatter around the mean, especially at cluster-scale masses, where simulations have historically suffered from lack of volume coverage. Predictions for the distribution of the concentration are particularly valuable since they can be used to check for selection biases in observations. As an example, if there is a concern that lensing-based searches are likely to be biased toward high-concentration halos, then, at a given mass bin, one can test for this bias by comparing to the predicted theoretical distribution. For this method to work, there should be enough objects at a given mass, a target that will be attained in the near future.

We have computed the concentration distribution for a large set of cosmologies, a subset of which we discuss here. Previous studies (Jing 2000; Shaw et al. 2006; Neto et al. 2007; Duffy et al. 2008) have fitted the concentration distribution to a log-normal distribution. However, this distribution is also very well described by a Gaussian as noted by Lukić et al. (2009) and Reed et al. (2011), consistent with the idea that the (mass-binned) concentration ensembles respect the central limit theorem. We have found that a Gaussian distribution provides a very good fit to our data, with relatively small non-Gaussian tails. As a representative example, we show the distribution of c_{200} (full halo sample at $z = 0$) for the mass bin centered at $1.5 \times 10^{14} h^{-1} M_\odot$ in Figure 3.

Assuming a Gaussian distribution, the standard deviation in the c - M relation can be calculated as

$$\sigma_c(M) = \sqrt{\frac{\sum_i c_i^2 M_i}{\sum_i M_i} - c(M)^2} \quad (8)$$

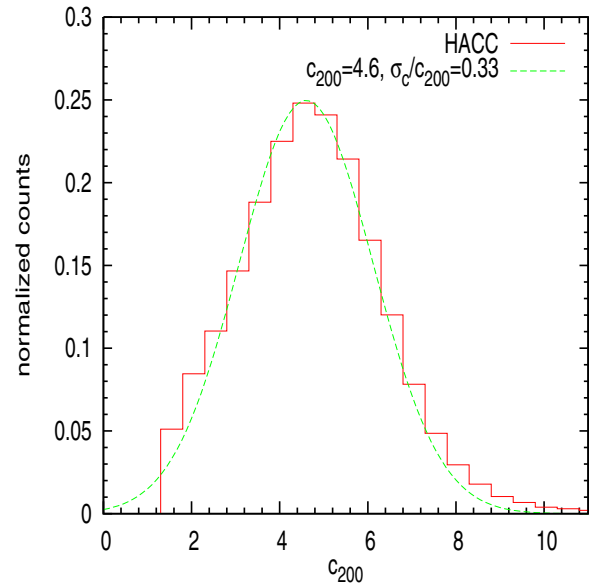


Figure 3. c - M distribution at a mass bin centered at $1.5 \times 10^{14} h^{-1} M_\odot$ using results from the HACC simulation at $z = 0$. The lines show a Gaussian distribution with standard deviation $\sigma_c/c \sim 0.33$.

(A color version of this figure is available in the online journal.)

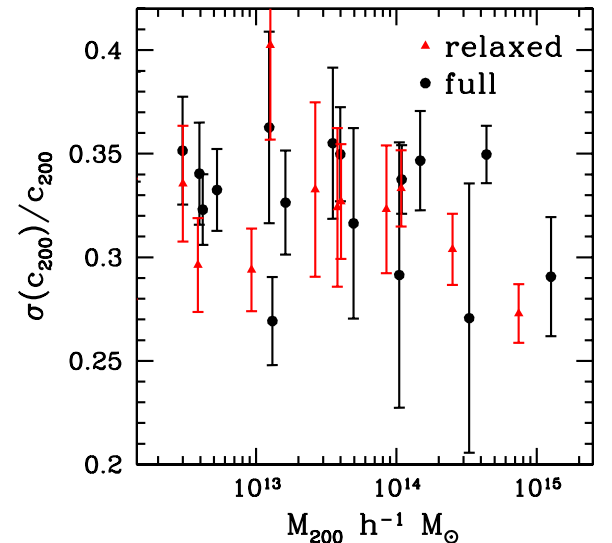


Figure 4. c_{200} - M_{200} distribution for the relaxed and full halo samples characterized by the ratio of the standard deviation to the mean value of c_{200} . All three redshifts are plotted. Note that σ_c/c shows no redshift evolution. The case of $\Delta = \Delta_{\text{vir}}$ shows identical behavior.

(A color version of this figure is available in the online journal.)

and the associated error in determining the scatter is the Poisson error in each bin as

$$\Delta \sum_c (M) = \sum_c (M) / \sqrt{N_i}, \quad (9)$$

where N_i is the number of halos in the mass bin with mass M . As illustrated in Figure 3 for the case of halos in the mass bin at $1.5 \times 10^{14} h^{-1} M_\odot$, at $z = 0$, the standard deviation of the Gaussian distribution is roughly $\sigma_c \simeq 0.33c$, over our mass and redshift range, with mild dependence on the mass at the very high mass end, such that for $M_{200} > 8 \times 10^{14} h^{-1} M_\odot$, $\sigma_c \simeq 0.28c$ (Figure 4). These results are in very good agreement

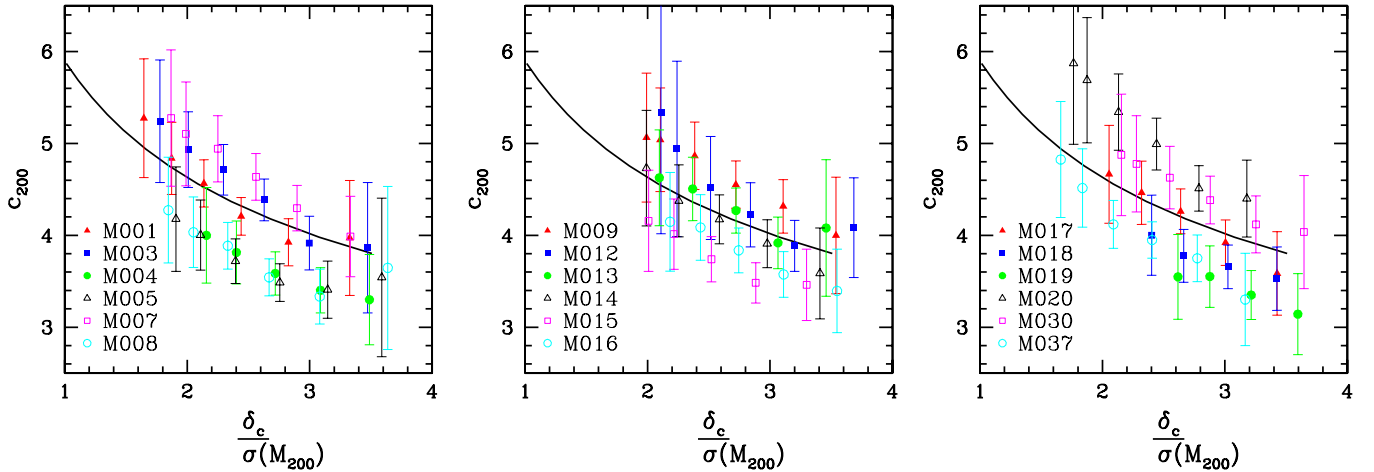


Figure 5. Mean c - M relation at $z = 0$ (full sample) when w CDM parameters are varied. The solid curve in all three panels is the fit to the reference Λ CDM cosmology as specified in Table 2.

(A color version of this figure is available in the online journal.)

with Reed et al. (2011), who find $\sigma_c \simeq 0.28c$ for an analysis of halos extracted from the MS.

If instead, for comparison purposes, we fit our concentration distribution using the log-normal function, we find that $\sigma(\log_{10}(c_{200})) = 0.16$ for the full sample, and 0.12 for the relaxed sample (this equivalent distribution is mildly skewed with respect to the data). These results may be compared to those of Duffy et al. (2008), who obtain 0.15 and 0.11, respectively, and to Neto et al. (2007) who find 0.14 and 0.1. Our scatter is therefore about 5%–10% higher than the results of Duffy et al. (2008) and Neto et al. (2007). As shown by Neto et al. (2007), the variance is at a minimum for the radial range $(0.05\text{--}1)R_{\text{vir}}$. As noted earlier, our fit to the halo profile is over the range $(0.1\text{--}1)R_{\text{vir}}$ which may account for the $\sim 7\%$ larger value of the standard deviation. This choice trades off a slight increase in scatter for robustness against systematic effects, as also previously discussed.

Figure 4 shows that the relation $\sigma_c \simeq 0.33c$ is more or less independent of mass, redshift, or the dynamical state of the halo; it also remains invariant when the cosmology is varied (Figure 6). This implies that the concentration scatter depends on cosmology, redshift, or the dynamical state, in essentially the same way as the mean concentration, confirming the initial finding of Dolag et al. (2004) from a small sample of simulated halos, but spanning multiple dark energy cosmologies. A more quantitative study of the distribution of concentrations will be presented elsewhere.

5. c - M RELATION FOR w CDM COSMOLOGIES

In this section we study how the halo profiles, and hence the concentration, vary with cosmology. We use 18 different runs, each with a volume of $(1.3 \text{ Gpc})^3$ and 1024^3 particles. The runs are carried out using GADGET-2 and each run has a different set of w CDM parameters. These simulations are a subset of the Coyote universe suite (see Heitmann et al. 2009 and Heitmann et al. 2010 for details). The simulation suite consists of 38 runs covering the 2σ range of w CDM parameter space as constrained by *Wilkinson Microwave Anisotropy Probe* (WMAP) five-year results (Komatsu et al. 2009). We choose 18 runs (plus the reference cosmology run) out of the 38 to show the cosmology dependence and retain the model numbering from the original Coyote runs. The runs have a coarser force

resolution than the GS and HACC simulations. The effect of this is considered in the Appendix, where it is shown that the G run has a systematically lower concentration compared to the HACC run over the same mass scale by about 5%–10% (Figure 11, left panel). To compensate for this minor underestimate, we rescale concentrations obtained from the w CDM runs by a factor of 1.05, checking for correctness by comparing against the fit obtained for the reference cosmology.

Figure 5 shows the variation of the c - ν relation with respect to the best-fit WMAP5 cosmology. The mean c - ν relation varies by about $\pm 20\%$ over the currently allowed w CDM cosmological parameter range. Note that ν already accounts for some of the cosmology dependence of the c - M relation, so a part of the variation is actually hidden. Since we have already found that expressing c as a function of ν explains the redshift evolution of NFW halo profiles, we illustrate the cosmology dependence using the c - ν relation in place of the c - M relation.

Table 3 shows the approximate difference between the (corrected) mean c - M relation seen in each of the w CDM runs compared to the mean c - M relation obtained for the reference Λ CDM cosmology. Note that although most of the variation in the c - M relation is in the overall amplitude, the slope also changes for some of the models (e.g., M003, M012). Interestingly, we find that some of the models show no variation compared to the reference, although these models differ across the range of cosmological parameters. For example, M014 and M017 both have lower σ_8 compared to the reference model, but show essentially no variation—parameters other than σ_8 are clearly also active. The standard deviation of the concentration distribution, on the other hand, changes in the same way as the mean, leaving the ratio σ_c/c almost universal (Dolag et al. 2004). Figure 6 shows that the σ_c/c varies by $< 5\%$ over the range of w CDM cosmologies.

Semianalytical “toy models” based on Press–Schechter arguments (Press & Schechter 1974) have attempted to model the cosmology and redshift dependence of halo concentrations via the underlying dependence on the matter power spectrum and the evolution history of the universe (Navarro et al. 1997; Eke et al. 2001; Bullock et al. 2001). The model of Navarro et al. (1997) has two free parameters. It defines the halo formation redshift by requiring that half of the final halo mass be in progenitors with masses of some fraction of the final mass. The characteristic density scale of the NFW profile is then set by

Table 3Parameters for the 18 Cosmological Models Used to Study the c - M Relation

No.	ω_m	ω_b	n_s	$-w$	σ_8	h	M ($10^{14} M_\odot$)	Variation (%)
1	0.1539	0.0231	0.9468	0.816	0.8161	0.5977	13.3	0
3	0.1324	0.0235	0.9984	0.874	0.8484	0.6763	9.96	+15
4	0.1381	0.0227	0.9339	1.087	0.7000	0.7204	4.42	-18
5	0.1358	0.0216	0.9726	1.242	0.8226	0.7669	7.20	-20
7	0.1268	0.0223	0.9210	0.700	0.7474	0.6189	7.30	+15
8	0.1448	0.0223	0.9855	1.203	0.8090	0.7218	8.04	-15
9	0.1392	0.0234	0.9790	0.739	0.6692	0.6127	4.98	+10
12	0.1223	0.0225	1.0048	0.971	0.6271	0.7396	2.26	+14
13	0.1482	0.0221	0.9597	0.855	0.6508	0.6107	4.78	+5
14	0.1471	0.0233	1.0306	1.010	0.7075	0.6688	5.42	0
15	0.1415	0.0230	1.0177	1.281	0.7692	0.7737	5.47	-15
16	0.1245	0.0218	0.9403	1.145	0.7437	0.7929	4.22	-10
17	0.1426	0.0215	0.9274	0.893	0.6865	0.6305	5.50	0
18	0.1313	0.0216	0.8887	1.029	0.6440	0.7136	3.05	-10
19	0.1279	0.0232	0.8629	1.184	0.6159	0.8120	1.88	-15
20	0.1290	0.0220	1.0242	0.797	0.7972	0.6442	8.24	+20
30	0.1234	0.0230	0.8758	0.777	0.6739	0.6626	4.09	+10
37	0.1495	0.0228	1.0233	1.294	0.9000	0.7313	11.7	-15

Notes. The second column from the right shows the mass corresponding to $\nu = 3$ for each cosmology at $z = 0$. The rightmost column shows the approximate variation of the mean c - M relation with respect to the reference run.

assuming it to be some multiple of the cosmic density at the redshift of halo formation. The mass fraction and the density multipliers are given by fitting to simulations. Bullock et al. (2001) modified this prescription by redefining the formation redshift as the redshift where the nonlinear mass scale M_* is some fraction of the final halo mass. They predicted the concentration as a multiple of the ratio of scale factors at the formation and collapse redshifts. Again, the fraction and multiplier are floating parameters, determined by fitting. Finally, Eke et al. (2001) used a single parameter (calibrated using simulations) to connect the collapse redshift with the effective amplitude of the power spectrum at cluster scales.

Even though the models reproduce the expected behavior of the c - M relation discussed in the Introduction, quantitatively their success has been decidedly mixed—results have been satisfactory over limited dynamic ranges when fitted to simulations, but tended to break down as the range is extended or cosmological parameters are varied. Particularly significant for us is the breakdown at large halo masses, characteristic of massive clusters at $z = 0$ (Neto et al. 2007; Gao et al. 2008; Duffy et al. 2008; Zhao et al. 2009), with a corresponding breakdown at lower masses, but at higher redshifts. Additionally, the redshift evolution of the c - M relation in the models is significantly stronger than is actually seen in simulations.

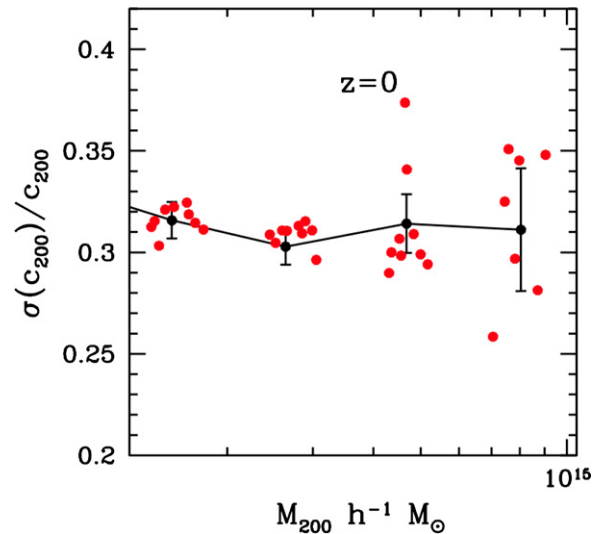


Figure 6. c_{200} - M_{200} distribution at $z = 0$ (full sample) when w CDM parameters are varied, following the characterization of Figure 4. The scatter is larger at high masses due to lower numbers of halos in high-mass bins. (A color version of this figure is available in the online journal.)

Although we have not attempted to optimize model parameters, the Eke et al. (2001) prescription agrees with our simulation results at 10%–20% accuracy for c_{200} for the Λ CDM cosmology (see Table 2 for the fit). We find that the prescriptions of Dolag et al. (2004; using a growth factor ratio multiplier) do not explain the cosmology variation in concentrations that we observe. For instance, in our case, the growth factor only varies by $<5\%$ over the range of simulations used, whereas the variations of concentrations seen is $\sim \pm 20\%$.

Regarding the modeling of the scatter in the concentration, it is natural to examine this in the context of different assembly histories for halos with the same mass (Wechsler et al. 2002; Zhao et al. 2003; see also Cohn & White 2005). However, in their MS analysis, Neto et al. (2007) find that the concentration scatter cannot be accounted for by differences in the time of formation alone. Additional consequences of environmental effects (Wechsler et al. 2006) appear to be important primarily for low-mass halos. Therefore, one is driven to the general conclusion that there is still no replacement for large-scale simulations if reliable predictions for halo concentrations and the distribution of concentrations are required.

6. COMPARISON WITH OBSERVATIONS

In this section, we compare our simulation results with some of the recent observations of the concentration–mass relation for clusters. The observational results span a variety of techniques,

Table 4
Observation Data Used in This Paper

Observation	Method	Rel./All	No. of Clusters	Redshift Range
Oguri et al.	Strong+Weak lensing	All	28	$0.28 < z < 0.64$
Okabe et al.	Weak lensing	All	30	$0.15 < z < 0.3$
Wojtak & Lokas	Kinematics	Rel.	41	$z < 0.1$
Vikhlinin et al.	X-ray	Rel.	19	$z < 0.2$
Schmidt & Allen	X-ray	Rel.	34	$0.06 < z < 0.7$
Buote et al.	X-ray	Rel.	26	$z < 0.23$
Ettori et al.	X-ray	All	44	$0.1 < z < 0.3$

Note. We use only objects with mass $> 5 \times 10^{13} h^{-1} M_\odot$ from Buote et al.

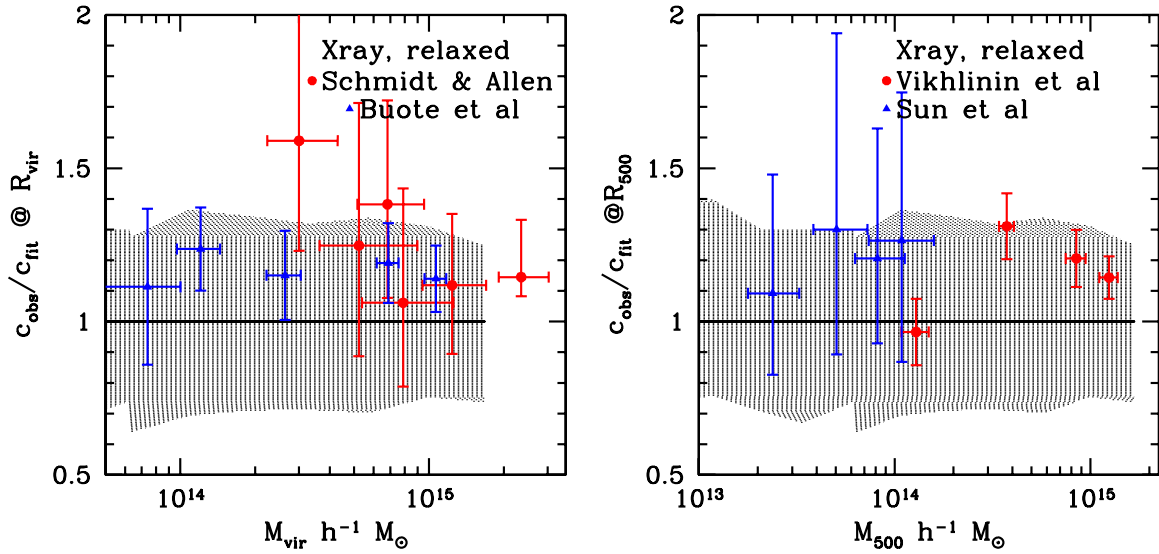


Figure 7. Ratio of observed concentration to theoretical predictions for relaxed cluster observations. The first two sets of data are taken from Schmidt & Allen (2007) and Buote et al. (2007; left panel, for details see the text). The shaded area represents the 1σ boundary for the theoretical predictions. The right panel shows the comparison against observations of the *Chandra* Cluster Cosmology Project (Vikhlinin et al. 2009). This data set includes updates to the results of Vikhlinin et al. (2006) and adds six new clusters (Table 5). Note that each data point actually represents observations of multiple clusters.

(A color version of this figure is available in the online journal.)

including strong and weak lensing (e.g., Comerford & Natarajan 2007; Broadhurst et al. 2008; Mandelbaum et al. 2008; Okabe et al. 2010; Oguri et al. 2012), X-ray observations of relaxed clusters (e.g., Buote et al. 2007; Vikhlinin et al. 2006; Schmidt & Allen 2007; Vikhlinin et al. 2009) and relaxed and unrelaxed clusters (Ettori et al. 2011), and cluster kinematics (e.g., Rines & Diaferio 2006; Wojtak & Lokas 2010). The datasets used are summarized in Table 4. Our aim is to provide a set of figures that enables the reader to judge by eye the current status of how well the theoretical predictions match against observations. Because there are significant observational systematics that are unclear and the observational statistics are still limited, we do not believe that a more complete statistical analysis is necessary, or even particularly useful. The strategy we follow is to take the ratio of each measured concentration to the theoretically predicted concentration at the object’s observed mass and redshift. We then bin in mass to show a relatively limited number of comparison points in each figure. Thus each point in the observation plots represents an average over ~ 5 data points. (The corresponding Poisson error bars use the improved formula $\sigma_{\pm} = \sqrt{N_h + 1/4} \pm 1/2$ as given by Heinrich 2003, which asymptotes to $\sqrt{N_h}$ at large N_h .)

We begin our comparison using results from X-ray observations of relaxed clusters as shown in Figure 7. Schmidt & Allen (2007) have measured the concentration of 34 dynamically relaxed clusters ($0.06 < z < 0.69$) from *Chandra* observations (left panel). The theoretical predictions are in good agreement for masses $M_{\text{vir}} > 4 \times 10^{14} h^{-1} M_{\odot}$, with minor tension at lower masses. The data presented by Buote et al. (2007) are a compilation of analyses of relaxed systems from *Chandra* and *XMM-Newton*; we show only the higher mass range, represented by results taken from Pointecouteau et al. (2005), Vikhlinin et al. (2006), Zappacosta et al. (2006), and Gastaldello et al. (2007), spanning a redshift range of $0.016 < z < 0.23$. All of these results are in very good agreement with the predictions, lying within the 1σ boundary. The right panel shows results from 19 clusters that were part of the *Chandra* Cluster Cosmology Project (Vikhlinin et al. 2009; $0.016 < z < 0.25$),

Table 5
Updated Masses and Concentrations from the *Chandra* Cluster Cosmology Project

Cluster	M_{500} (M_{\odot})	δM (M_{\odot})	c_{500}	$+\delta_c$	$-\delta_c$	z
a133	3.166×10^{14}	3.776×10^{13}	3.15	0.29	0.28	0.0569
a262	8.310×10^{13}	7.272×10^{12}	3.48	0.30	0.30	0.0162
a383	3.049×10^{14}	3.100×10^{13}	4.31	0.42	0.40	0.1883
a478	7.668×10^{14}	1.010×10^{14}	3.57	0.27	0.26	0.0881
a907	4.623×10^{14}	3.790×10^{13}	3.46	0.42	0.42	0.1603
a1413	7.569×10^{14}	7.550×10^{13}	2.93	0.18	0.17	0.1429
a1795	6.009×10^{14}	5.134×10^{13}	3.21	0.18	0.18	0.0622
a1991	1.235×10^{14}	1.654×10^{13}	4.31	0.34	0.34	0.0592
a2029	8.147×10^{14}	7.674×10^{13}	4.04	0.21	0.21	0.0779
a2390	1.077×10^{14}	1.092×10^{14}	1.66	0.13	0.13	0.2302
cl1159	1.056×10^{14}	2.578×10^{13}	1.77	0.38	0.24	0.0810
MKW4	7.734×10^{13}	1.032×10^{13}	2.54	0.16	0.14	0.0199
a2717	1.478×10^{14}	2.134×10^{13}	2.69	0.19	0.19	0.0498
a3112	3.448×10^{14}	3.097×10^{13}	4.47	0.28	0.27	0.0761
a1835	1.245×10^{15}	1.342×10^{14}	2.81	0.17	0.17	0.2520
a1650	4.683×10^{14}	1.736×10^{13}	3.74	0.19	0.19	0.0846
a2107	2.361×10^{14}	3.928×10^{13}	3.38	0.28	0.25	0.0418
a4059	3.496×10^{14}	2.691×10^{13}	2.95	0.09	0.09	0.0491
rxj1504	1.068×10^{15}	1.768×10^{14}	3.16	0.38	0.38	0.2169

Notes. δM is the estimated error in the mass, and $+\delta_c$ and $-\delta_c$ are the upper and lower error bounds for the concentrations. The masses are for $h = 0.72$.

the data set represented in Table 5, for which the concentration measurements were not previously reported. Once again, the agreement is excellent. Overall, we conclude that comparisons with X-ray measurements of relaxed clusters are in good accord with (concordance) Λ CDM predictions.

Next we turn to the results of Ettori et al. (2011) who measured the concentrations of 44 X-ray luminous clusters ($0.09 < z < 0.31$) using *XMM-Newton* (Figure 8). Their sample contains both relaxed and unrelaxed clusters. As with the Schmidt & Allen (2007) comparison, we find that the simulation results are in good agreement with these observations

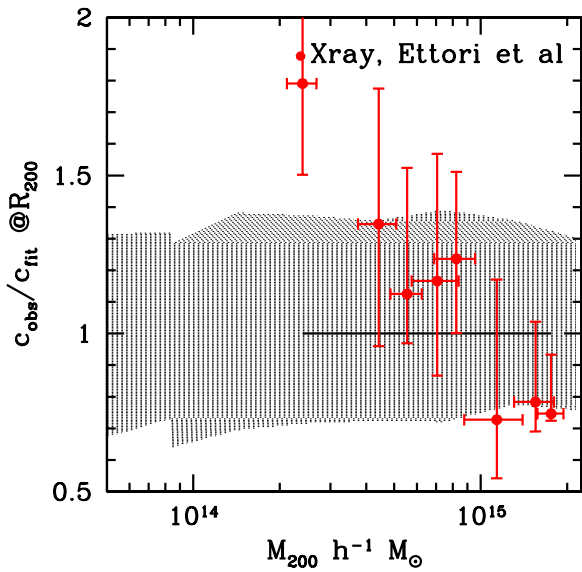


Figure 8. Ratio of observed concentration to theoretical predictions for the *XMM-Newton* cluster observations of Ettori et al. (2011). The shaded area represents the 1σ boundary for the theoretical predictions. Each data point actually represents observations of multiple clusters.

(A color version of this figure is available in the online journal.)

for $M_{200} > 4 \times 10^{14} h^{-1} M_{\odot}$. As the authors note, a slope cannot be fitted to their data because of the narrow mass range of the observations relative to their errors. Thus, we regard the current level of agreement as being quite satisfactory.

We now consider lensing measurements of cluster profiles using weak and strong lensing and combinations thereof. Figure 9 shows the comparison of the theoretical predictions against the results of LoCuSS, a weak lensing study of 30 clusters with Subaru/Suprime-Cam imaging data (Okabe et al. 2010) and a combined strong and weak lensing analysis of 28 clusters from the Sloan Giant Arcs Survey (Oguri et al. 2012). The left panel of Figure 9 shows the weak lensing results displayed in the

same manner as for the X-ray data sets. The results from Okabe et al. (2010) are in excellent agreement with our predictions, completely consistent with the corresponding measurements from relaxed clusters. The results of Oguri et al. (2012) are consistent with our predictions for $M_{\text{vir}} > 4 \times 10^{14} h^{-1} M_{\odot}$, but at lower masses there appears to be a significant discrepancy with a much steeper c - M dependence. Although baryon cooling may play a role at smaller masses, there is no convincing reason for such a large effect—for which there is no signal in the X-ray data (or in the simulations of Duffy et al. 2010). Note that the target selection in the two surveys is quite different, that of Okabe et al. (2010) being essentially volume-limited, while any strong-lensing selected sample such as that of Oguri et al. (2012) must have a significant amount of selection and projection bias (Rozo et al. 2008; Meneghetti et al. 2010). Note also that an analysis based on mock weak lensing observations in the MS (Bahé et al. 2012) has shown that there is bias in weak lensing measurements of concentration as well, tending to depress the measured concentration by a small amount from the predicted value.

The right panel of Figure 9 shows the combined strong plus weak lensing analysis including a model for lensing bias (Oguri et al. 2012). Processing the results through the lensing bias model (by enhancing the theoretical prediction) brings down the discrepancy significantly but there is still evident tension for masses $M_{\text{vir}} < 4 \times 10^{14} h^{-1} M_{\odot}$. Nevertheless, we note that there is a clear trend of lensing concentrations reducing over time and becoming more consistent with the theoretical predictions. Other data which our results appear to be in agreement with can be found in Comerford & Natarajan (2007; strong lensing) and Coe et al. (2012; strong and weak lensing). A cautionary note regarding weak lensing concentration measurements of clusters is provided in Figure 6 of Comerford & Natarajan (2007) regarding A1689 and in the results given in Israel et al. (2011) as part of the *400d* weak lensing survey.

Instead of using individual objects, a stacked statistical analysis can be applied to clusters, as carried out using Sloan Digital Sky Survey (SDSS) data by Mandelbaum et al. (2008),

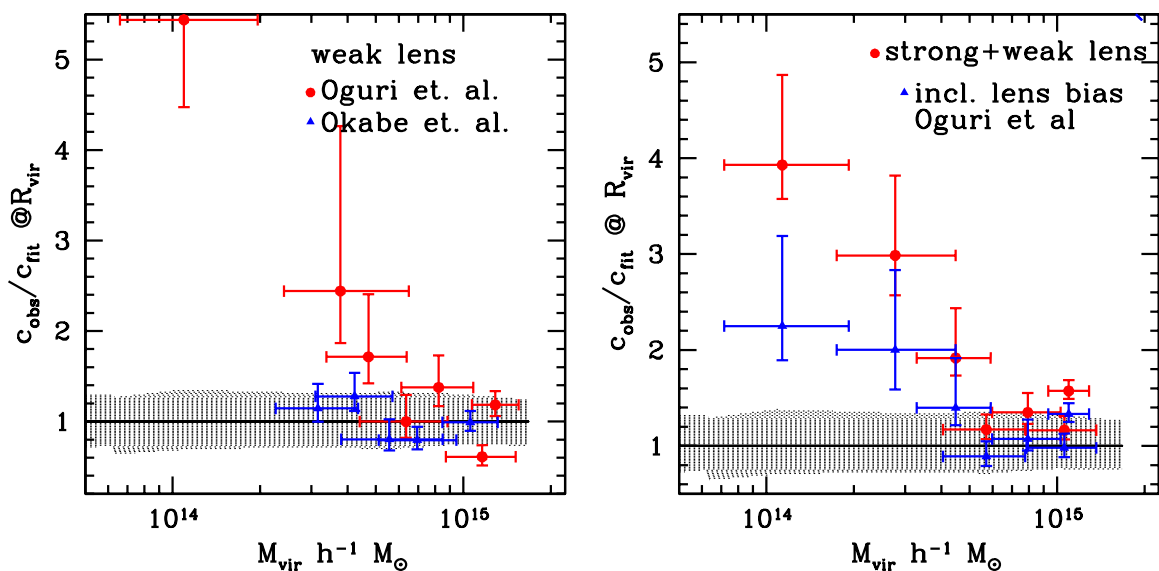


Figure 9. Theoretical vs. observed c - M relation for weak and strong lensing. The left panel shows weak lensing data from Okabe et al. (2010) and Oguri et al. (2012). The Okabe et al. (2010) results are in very good agreement with the predictions, while the Oguri et al. (2012) results are strongly discrepant at the low-mass end. The right panel shows the combined strong and weak lensing results from Oguri et al. (2012) including their bias model-corrected prediction (blue). The correction reduces the discrepancy significantly but some tension remains below $\sim 4 \times 10^{14} h^{-1} M_{\odot}$.

(A color version of this figure is available in the online journal.)

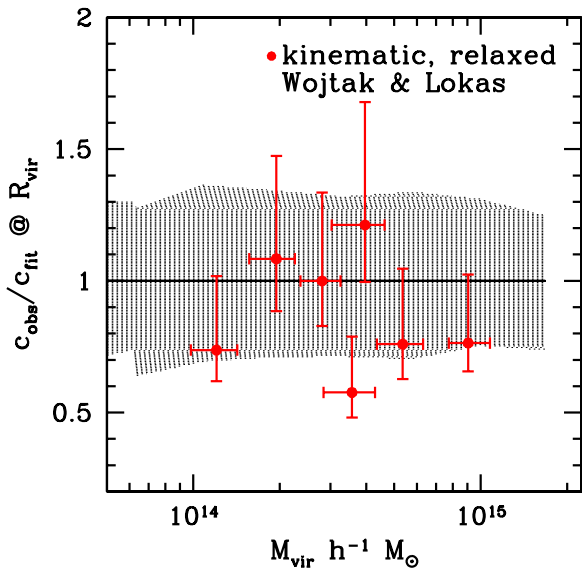


Figure 10. Ratio of measured to predicted concentrations; the data are taken from the results of a projected phase space analysis by Wojtak & Lokas (2010). (A color version of this figure is available in the online journal.)

reaching cluster masses of $\sim 6 \times 10^{14} h^{-1} M_{\odot}$. This analysis finds no evidence for a major boost in concentration at lower masses and the final result— $c_{200b} \sim 4.6 \pm 0.7$ at $\langle z \rangle = 0.22$ at a mass of $M_{200b} \sim 10^{14} h^{-1} M_{\odot}$ is 20%–40% less than our prediction of $c_{200b} \sim 6.5$ at the corresponding mass. The mild c – M dependence they observe is, however, in good agreement with our predictions— ~ 0.09 compared to the observed slope of 0.13 ± 0.07 .

Finally, we consider the estimates of the concentration using galaxy kinematics in clusters. Rines & Diaferio (2006) matched X-ray cluster catalogs with SDSS and used infall patterns to compute cluster mass profiles. The c_{200} concentration has significant scatter—values ranging from 5 to 17—but their best-fit average profile, with fits restricted to $r \leq R_{200}$, yields $c_{200} = 5.2$ which, at an average mass of $M_{200} \simeq 10^{14} h^{-1} M_{\odot}$, is in agreement with our predictions. More recently, Wojtak & Lokas (2010) have published an analysis of 41 relaxed galaxy clusters ($0.013 < z < 0.095$); we compare our predictions with their results in Figure 10. Although their data have considerable scatter, these are in quite reasonable agreement with the predictions from simulations. Thus, despite possible systematic difficulties with such methods (see, e.g., White et al. 2010), the current results are in reasonable accord with theoretical expectations.

7. SUMMARY AND DISCUSSION

We presented results for the concentrations of dark matter halos using a set of large-volume simulations. With a total volume roughly 1–2 orders of magnitude larger compared to previous simulations, we focused on studying the c – M relation for massive clusters. As shown in the past, at the high-mass end, the c – M relation becomes flatter at $z = 0$ and the flattening becomes more significant at higher z . The mean concentration of the sample when expressed in terms of the peak height parameter, $\nu(M, z) = \delta_c / \sigma(M, z)$, shows a roughly uniform slope at all redshifts. Indeed, the slope of the c – ν relation does not change with redshift. The amplitude of the c – ν relation evolves by about 30% at the high-mass end from $z = 0$ to 2. The z -evolution is consistent with the results of Gao et al.

(2008), although the overall amplitude of the concentration differs because of the different choices of σ_8 . We do not observe a rise in concentration at higher masses as reported by Klypin et al. (2011) and Prada et al. (2012; the Appendix includes further discussion).

Our large halo sample allows us to study the distribution of the concentration in individual mass bins; we find that the distribution of concentrations is well described by a Gaussian PDF (Lukić et al. 2009; Reed et al. 2011). Thus the halo profile shape can be described by two parameters—the mean concentration and its standard deviation. By comparing results across a number of w CDM cosmologies, we find that the standard deviation is roughly universal, $\sigma_c \simeq c/3$, and more or less independent of redshift, halo dynamical state, or cosmological parameters.

We investigated how the concentration changes as the cosmological parameters are varied by using a set of 18 runs spanning the w CDM cosmology parameter space. The parameter range covers the 2σ variation around the best-fit WMAP5 cosmology. We find that over this range, the c – M relation varies by approximately $\pm 20\%$, but the standard deviation σ_c still follows the relation $\sigma_c = 0.33c$. As suggested by our work on the w CDM models and also previous studies of redshift evolution, the halo formation epoch, and hence the concentration, depends on the matter fluctuations, slope of the power spectrum, and the growth factor. Thus calibrating the c – M relation as a function of cosmology is important for a wide variety of problems, ranging from galaxy formation, the weak lensing shear power spectrum, to the case of assembly bias in clusters. We will address the cosmology dependence of the c – M relation in detail using more simulations and analytical models elsewhere.

The simulation predictions are in good agreement with observations from strong lensing, weak lensing, galaxy kinematics, and X-ray data for massive clusters with masses $M_{\text{vir}} > 4 \times 10^{14} h^{-1} M_{\odot}$. At lower masses, different observations suffer from different sources of systematic error. For example, the lensing data need to account for bias due to the triaxiality of halos while the X-ray data typically ignore the non-thermal pressure component in galaxy clusters which can lead to a systematic underestimate of the cluster mass (Lau et al. 2009). The simulations, on the other hand, also need to account for baryonic effects which play a bigger role as the halo mass decreases. As a result, due to cooling, gravity-only simulations may predict 20%–30% lower concentration for clusters with masses $M_{\text{vir}} < 4 \times 10^{14} h^{-1} M_{\odot}$. The fact that most recent observations are in agreement with the simulation results (and amongst themselves) to better than 20% for massive clusters ($M_{\text{vir}} > 4 \times 10^{14} h^{-1} M_{\odot}$) indicates that baryonic effects influencing the cluster mass profile are indeed small and that the individual observational systematics are under some level of control.

It is a pleasure to acknowledge discussions and collaborations with Joanne Cohn, Zarija Lukić, Darren Reed, Alexey Voevodkin, and Martin White. We acknowledge several motivating conversations with Masahiro Takada (S.H.) and Mike Gladders (S.H. and K.H.). We thank Volker Springel for discussions and for making GADGET-2 publicly available. We are indebted to Patricia Fasel and Adrian Pope for their contributions to the HACC analysis framework. We thank Anatoly Klypin and Francisco Prada for pointing out a numerical error in an earlier version of the Appendix (now corrected) and for discussions of results obtained by our two groups. A special acknowledgment is due to the resource allocation awarded to us on the

hybrid supercomputer Cerrillos and other clusters under the Los Alamos National Laboratory Institutional Computing initiative. Part of this research was supported by the DOE under contract W-7405-ENG-36. The authors acknowledge support from the LDRD programs at Los Alamos National Laboratory and Argonne National Laboratory, where analysis was performed on the Eureka cluster. S.B. and K.H. were supported in part by NASA.

APPENDIX

SYSTEMATICS AND ROBUSTNESS CHECKS

In this Appendix, we investigate various sources of possible systematic errors in determining halo concentrations. We note that the simulations were carried out keeping in mind error control requirements on force-resolution, time-stepping errors, and mass resolution that have been spelled out in the literature (Tormen et al. 1997; Power et al. 2003; Heitmann et al. 2008; Lukić et al. 2007).

We locate halo centers by using a very fast FOF method. In principle, there is a very mild selection effect induced by the choice of linking length—if the FOF finder links two halos, then only the higher density center of one halo will be used and the other halo will be statistically lost (see, e.g., Figure 12 in Lukić et al. 2009). A smaller linking length would in effect free up the other halo as well, although it would slow down the center-finding algorithm. In practice, however, this is not an issue given the fact that individual concentrations need to be extracted with small errors. To do so we use a minimum number of ~ 2000 particles per halo; tests have shown that with more than 500 particles per halo, there is excellent agreement between our method of halo finding and conventional spherical overdensity halo finders (Knebe et al. 2011).

Another problem with halo center finding is miscentering, which in general will tend to reduce the concentration. To produce a quantitative estimate for this effect, we consider an extreme example by offsetting the center of every halo by $30 h^{-1}$ kpc (a value of the same order as the force resolution) and recomputing the profile of every halo in the G run. As shown in Figure 11, left panel, randomly offsetting the center by this amount reduces the c - M relation by about 10% at $M_{200} = 5 \times 10^{13} h^{-1} M_{\odot}$ with the difference vanishing toward the high-mass end. (This sort of misestimation is more relevant to analyses with stacked halos.)

The halo mass profiles were fitted using 20 bins, linear in mass (cf. Equation (3)). We rechecked some of the profiles using logarithmic binning at two extremes of halo masses ($5 \times 10^{12} h^{-1} M_{\odot}$ and $5 \times 10^{14} h^{-1} M_{\odot}$) finding a small, more or less random difference at the 3%–6% level for the best-fit concentration, which may be compared to the actual error spread of 15%–25% for the individual halos.

For profile tests across the different runs, we begin by comparing the GS and HACC runs (left panel of Figure 11). Note that although these runs have been carried out with completely different codes, the data for c_{200} go over smoothly from one mass range to another. (GADGET-2 and HACC were run with roughly similar force resolution.) The G runs were originally carried out for a different purpose, hence their force resolution is somewhat lower. As expected, this has the consequence of mildly reducing the concentration (Tormen et al. 1997; Power et al. 2003) by about 5%.

We have tested our profile-fitting procedure by generating Monte Carlo NFW profile samples using different numbers of

particles; with the particle numbers used to sample halos kept larger than 2000, the method was accurate to a few percent (worst case) and superior to simpler methods based on radius ratios and variants thereof. To investigate how other parameters could affect concentration values, we went back to using the halos from the simulations. The right panel of Figure 11 shows the effect of varying the range of the halo profile used to fit to the NFW form. Changing the starting radius from $r = 0.1 R_{\text{vir}}$ to $r = 0$, with the outer limit fixed at $r = R_{\text{vir}}$ reduces the overall c - M relation by about 5% (resolution/particle undersampling limitations). Fixing the starting radius at $0.1 R_{\text{vir}}$ but changing the stopping radius to $2 R_{\text{vir}}$ changes the relation only by a negligible amount as compared to the fiducial range $(0.1-1)R_{\text{vir}}$. Reducing the stopping radius to $0.5 R_{\text{vir}}$ steepens the c - M relation by about 10%.

Because our primary interest is in halos that have mass significantly in excess of M_* , it is important to ask what possible systematic effects could arise from fitting such objects without paying attention to their infall structure (substructure in the outer part of the halo). The average radial velocity of a halo fluctuates around zero out to an infall radius, r_{inf} , beyond which it goes negative, this transition roughly defining the boundary of the infall region. Purely as an informal nomenclature, we refer to the region internal to the infall radius as the virialized region. We find all halos that have (the formal) $R_{\text{vir}} > r_{\text{inf}}$ and exclude them from the analysis, thus focusing attention on halos that have much less infall contamination. The result is shown by the solid line in the right panel of Figure 11. Not unexpectedly, cluster size halos with masses $\sim 10^{14} h^{-1} M_{\odot}$ and greater are much more sensitive to this cut and display an enhancement of the c - M relation by about 10% when only the “virialized” subsample is used.

As mentioned in Section 2, the halo concentration can be measured in different ways, even if one sticks to the NFW definition(s) of concentration. Therefore, it is important to investigate what sources of uncertainty can arise from using different definitions that may be mathematically equivalent, but not operationally the same. Here we study two alternative independent techniques for measuring concentrations—the radius ratio and the maximum circular velocity. The radius ratio method is very simple: We measure the radius at $\Delta = 300$ and 200 for each halo in our sample. Then, assuming the halos are described by an NFW profile, the radius ratio is given by

$$\frac{300R_{300}^3}{200R_{200}^3} = \frac{m(c_{200}R_{300}/R_{200})}{m(c_{200})}, \quad (\text{A1})$$

where $m(x) = \ln(1+x) - x/(1+x)$. Given a measurement of R_{300}/R_{200} , one solves the nonlinear equation (A1) for c_{200} . The mean c - M relation is then obtained in the same way as for profile fitting. The left panel of Figure 12 shows the concentration measured using the profile fit and by the radius ratios. For this test we focused on the relaxed sample, although the full sample gave identical results. The diagonal line in the figure denotes the ideal exact agreement of the concentration measures from the profile fit and from the radius ratio. As the results in the figure show, the two methods agree quite well within the specified errors. The error in the concentration measurement using the radius ratio arises from the error in determining the radii—the Poisson error from the total number of particles inside R_{300} and R_{200} . As expected, the radii are determined quite accurately as there are large number of particles inside these radii, but because of the logarithmic nature

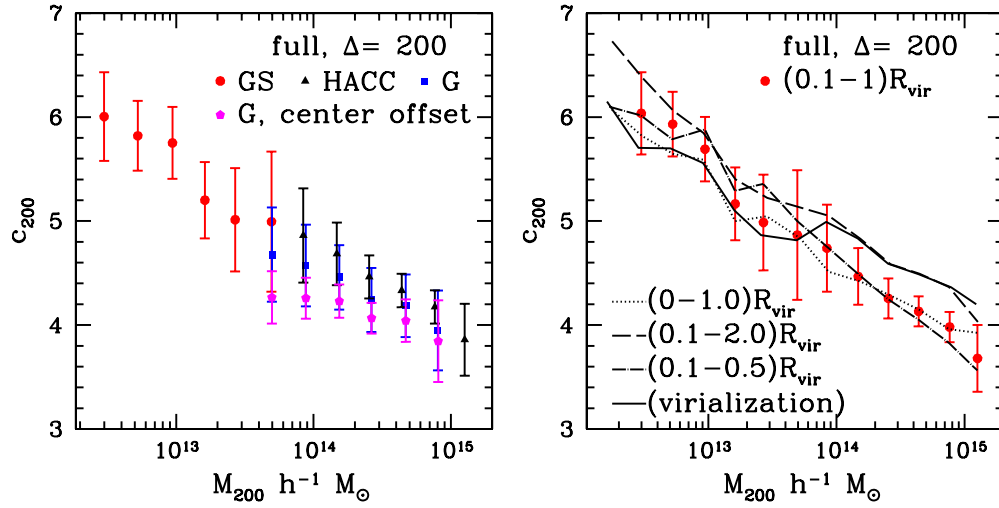


Figure 11. Tests to identify possible sources of systematic error. The left panel shows the three runs used in this paper and how the force resolution affects concentration measurements. There is excellent agreement between the GS and HACC runs, even though they were run using two completely different codes with different settings. The lower-resolution G run (resolution = $35 h^{-1}$ kpc) is systematically lower by about 5% compared to the HACC run (resolution = $7 h^{-1}$ kpc). We also study the possible effect of a misestimate of the halo center for the G run which can lead to a further reduction of concentration values. The right panel studies two other systematic issues: (1) the profile range used for fitting and (2) effect on concentration measurements when halos with large radial infall velocity are removed from the sample (solid curve). See the text for further discussion.

(A color version of this figure is available in the online journal.)

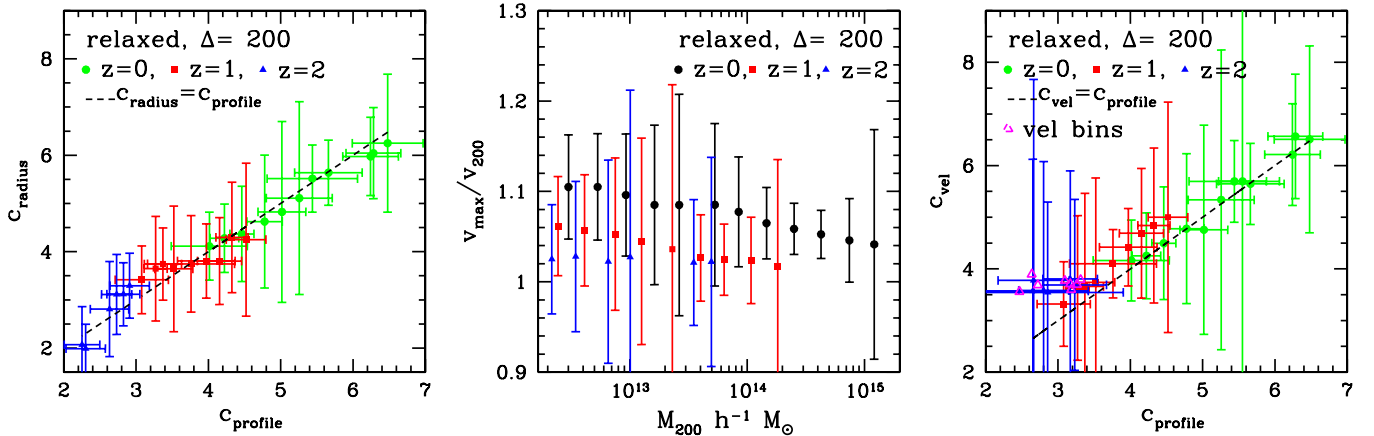


Figure 12. Comparison (left and right panels) between c_{200} measured for relaxed clusters using profile fitting and that obtained from the radius ratio (left panel) and v_{max}/v_{200} (right panel). The diagonal line represents the ideal case when the measured concentrations agree exactly. The middle panel shows the ratio of the maximum circular velocity to that at radius R_{200} for $z = 0$ for the relaxed sample as a function of mass. Note the smooth crossover between the GS and HACC runs at $M_{200} \sim 10^{14} h^{-1} M_{\odot}$ at redshifts $z = 0, 1$ (cf. Figure 1).

(A color version of this figure is available in the online journal.)

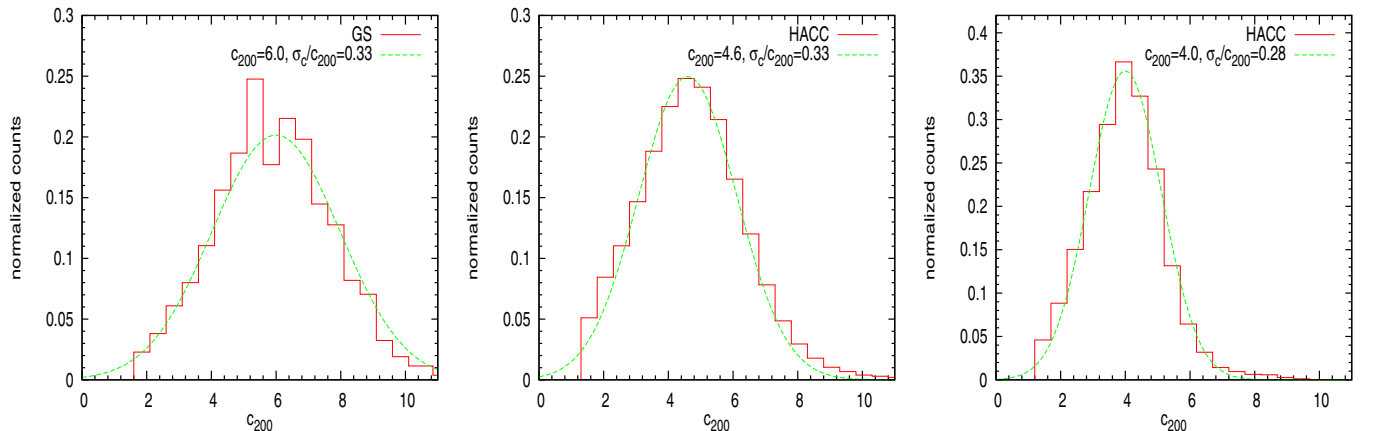


Figure 13. c - M distribution at three mass bins— $M_{200} = 5 \times 10^{12} h^{-1} M_{\odot}$ (left from the GS run), $1.5 \times 10^{14} h^{-1} M_{\odot}$ (middle, HACC), and $8 \times 10^{14} h^{-1} M_{\odot}$ (right, HACC)—from the halos drawn from the full sample at $z = 0$. Lines show the Gaussian distribution with standard deviation $\sigma_c/c \sim 0.33$ in the left and center panels, and $\sigma_c/c \sim 0.28$ in the rightmost panel.

(A color version of this figure is available in the online journal.)

of Equation (A1), the Δc_{200} become non-negligible. The error on the mean concentration also includes the Poisson error due to the finite number of halos in the individual mass bins.

The second method we investigate relies on using a proxy for the maximum circular velocity of a halo (Klypin et al. 2011; Prada et al. 2012). The circular velocity is given by

$$v^2 = GM(< r)/r. \quad (\text{A2})$$

For each halo in the sample we determine the maximum value of $v_{\text{max}}^2 = \max[GM/r]$ indirectly by using the halo's mass profile to determine the right-hand side of Equation (A2), and then divide by $v_{200}^2 = GM_{200}/R_{200}$. Assuming an NFW form, one can relate $v_{\text{max}}^2/v_{200}^2$ to the concentration, c_{200} ,

$$\frac{v_{\text{max}}^2}{v_{200}^2} = \frac{0.2162c_{200}}{m(c_{200})} \quad (\text{A3})$$

and solve for c_{200} . The middle panel of Figure 12 shows the ratio v_{max}/v_{200} as a function of M_{200} for three redshifts for the relaxed cluster sample. The right panel compares the concentrations obtained from the maximum velocity method and profile fitting. Again, the methods agree quite well within the error estimates, the velocity method being noisier. The middle panel of Figure 12 shows the ratio v_{max}/v_{200} as a function of mass. Note that we cross over very smoothly from the GS run to the HACC run at $M_{200} = 10^{14} h^{-1} M_{\odot}$, more evidence for an excellent match between the results from these two simulations. One problem with this method is that because $r_{\text{max}} \sim 2.2r_s$ (where r_{max} is the radius where v reaches v_{max}), at low concentrations, r_{max} becomes very close to r_{Δ} , and is therefore very sensitive to any noise in the data, which will (1) result in biasing the concentration to a higher value (as seen in the flattening of the data at $c \sim 3$ in Figure 12, right panel) and (2) make the result very sensitive to the shape of the measured profile at $r \sim r_{\Delta}$, increasing the possibility of systematic errors. Finally, Klypin et al. (2011) and Prada et al. (2012) have both found that the maximum velocity method (along with their halo selection) leads to an upturn in the c - M relation at the high-mass end at higher redshifts. We are unable to confirm this effect in our measurements, where we can investigate it ($z = 1, 2$), but will return to it in forthcoming work.

We provide more information regarding the distribution of the concentrations, c_{200} , for the full halo sample at $z = 0$ by considering three representative mass bins, $M_{200} = 5 \times 10^{12} h^{-1} M_{\odot}$, $1.5 \times 10^{14} h^{-1} M_{\odot}$, and $8 \times 10^{14} h^{-1} M_{\odot}$, as shown in Figure 13. Previous studies (Jing 2000; Shaw et al. 2006; Neto et al. 2007; Duffy et al. 2008) fitted the concentration distribution to a log-normal form. However, this distribution is also very well described by a Gaussian as noted by Lukić et al. (2009) and Reed et al. (2011). Figure 13 shows that a Gaussian distribution provides a very good fit to our data (which has very little skewness), with negligible non-Gaussian tails.

We conclude that while statistical errors on the concentration-mass relation may have achieved $\sim 5\%$ accuracy in recent simulation studies, systematic uncertainties of the order of 10% are apparently difficult to avoid.

REFERENCES

- Bahé, Y. M., McCarthy, I. G., & King, L. J. 2012, *MNRAS*, 421, 1073
 Bhattacharya, S., Heitmann, K., White, M., et al. 2011, *ApJ*, 732, 211
 Broadhurst, T., Umetsu, K., Medezinski, E., Oguri, M., & Rephaeli, Y. 2008, *ApJL*, 685, L9
 Bryan, G. L., & Norman, M. L. 1998, *ApJ*, 495, 80
 Bullock, J. S., Kolatt, T. S., Sigad, Y., et al. 2001, *MNRAS*, 321, 559
 Buote, D. A., Gastaldello, F., Humphrey, P. J., et al. 2007, *ApJ*, 664, 123
 Coe, D., Umetsu, K., Zitrin, A., et al. 2012, *ApJ*, 757, 22
 Cohn, J. D., & White, M. 2005, *Aph*, 24, 316
 Comerford, J. M., & Natarajan, P. 2007, *MNRAS*, 379, 190
 Cui, W., Borgani, S., Dolag, K., Murante, G., & Tornatore, L. 2012, *MNRAS*, 423, 2279
 Diaferio, A., Geller, M. J., & Rines, K. J. 2005, *ApJL*, 628, L97
 Dolag, K., Bartelmann, M., Perrotta, F., et al. 2004, *A&A*, 416, 853
 Duffy, A. R., Schaye, J., Kay, S. T., & Dalla Vecchia, C. 2008, *MNRAS*, 390, L64
 Duffy, A. R., Schaye, J., Kay, S. T., et al. 2010, *MNRAS*, 405, 2161
 Eke, V. R., Navarro, J. F., & Steinmetz, M. 2001, *ApJ*, 554, 114
 Ettori, S., Gastaldello, F., Leccardi, A., et al. 2011, *A&A*, 526, 1
 Evrard, A. E., Bialek, J., Busha, M., et al. 2008, *ApJ*, 672, 122
 Gao, L., Navarro, J. F., Cole, S., et al. 2008, *MNRAS*, 387, 536
 Gastaldello, F., Buote, D. A., Humphrey, P. J., et al. 2007, *ApJ*, 669, 158
 Habib, S., Morozov, V., Finkel, H., et al. 2012, arXiv:1211.4864
 Habib, S., Pope, A., Lukić, Z., et al. 2009, *JPhCS*, 180, 012019
 Hamming, R. W. 1998, *Digital Filters* (Mineola, NY: Dover)
 Hayashi, E., & White, S. D. M. 2008, *MNRAS*, 388, 2
 Heinrich, J. 2003, *Coverage of Error Bars for Poisson Data* (CDF note 6438; Batavia; Fermilab)
 Heitmann, K., Higdon, D., White, M., et al. 2009, *ApJ*, 705, 156
 Heitmann, K., Lukić, Z., Fasel, P., et al. 2008, *CS&D*, 1, 1
 Heitmann, K., Ricker, P. M., Warren, M. S., & Habib, S. 2005, *ApJS*, 160, 28
 Heitmann, K., White, M., Wagner, C., Habib, S., & Higdon, D. 2010, *ApJ*, 715, 104
 Israel, H., Erben, T., Reiprich, T. H., et al. 2011, *A&A*, 546, A79
 Jing, Y. P. 2000, *ApJ*, 535, 30
 Jing, Y. P., & Suto, Y. 2002, *ApJ*, 574, 538
 Kazantzidis, S., Kravtsov, A. V., Zentner, A. R., et al. 2004, *ApJL*, 611, L73
 King, L., & Mead, J. 2011, *MNRAS*, 416, 2539
 Klypin, A. A., Trujillo-Gomez, S., & Primack, J. 2011, *ApJ*, 740, 102
 Knebe, A., Knollmann, S. R., Muldrew, S. I., et al. 2011, *MNRAS*, 415, 2293
 Komatsu, E., Dunkley, J., Nolte, M. R., et al. 2009, *ApJS*, 180, 330
 Komatsu, E., Smith, K. M., Dunkley, J., et al. 2011, *ApJS*, 192, 18
 Lau, E. T., Kravtsov, A. V., & Nagai, D. 2009, *ApJ*, 705, 1129
 Lawrence, E., Heitmann, K., White, M., et al. 2010, *ApJ*, 713, 1322
 Lewis, A., Challinor, A., & Lasenby, A. 2000, *ApJ*, 538, 473
 Lukić, Z., Heitmann, K., Habib, S., Bashinsky, S., & Ricker, P. M. 2007, *ApJ*, 671, 1160
 Lukić, Z., Reed, D., Habib, S., & Heitmann, K. 2009, *ApJ*, 692, 217
 Macciò, A. V., Dutton, A. A., & van den Bosch, F. C. 2008, *MNRAS*, 391, 1940
 Macciò, A. V., Dutton, A. A., van den Bosch, F. C., et al. 2007, *MNRAS*, 378, 55
 Mandelbaum, R., Seljak, U., & Hirata, C. M. 2008, *JCAP*, 08, 006
 Meneghetti, M., Fedeli, C., Pace, F., Gottlöber, S., & Yepes, G. 2010, *A&A*, 519, A90
 Mo, H. J., van den Bosch, F. C., & White, S. D. M. 2010, *Galaxy Formation and Evolution* (Cambridge: Cambridge Univ. Press)
 More, S., Kravtsov, A. V., Dalal, N., & Gottlöber, S. 2011, *ApJS*, 195, 4
 Navarro, J. F., Frenk, C. S., & White, S. D. M. 1996, *ApJ*, 462, 563
 Navarro, J. F., Frenk, C. S., & White, S. D. M. 1997, *ApJ*, 490, 493
 Neto, A. F., Gao, L., Bett, P., et al. 2007, *MNRAS*, 381, 1450
 Newman, A. B., Treu, T., Ellis, R. S., et al. 2012, arXiv:1209.1391v1
 Oguri, M., Bayliss, M. B., Dahle, H., et al. 2012, *MNRAS*, 420, 3213
 Okabe, N., Takada, M., Umetsu, K., Futamase, T., & Smith, G. P. 2010, *PASJ*, 62, 811
 Pointecouteau, E., Arnaud, M., & Prat, G. W. 2005, *A&A*, 435, 1
 Pope, A., Habib, S., Lukić, Z., Daniel, D., et al. 2010, *CSE*, 12, 17
 Power, C., Navarro, J. F., Jenkins, A., et al. 2003, *MNRAS*, 338, 14
 Prada, F., Klypin, A. A., Cuesta, A. J., Betancort-Rijo, J. E., & Primack, J. 2012, *MNRAS*, 423, 3018
 Press, W. H., & Schechter, P. 1974, *ApJ*, 187, 425
 Reed, D. S., Koushiappas, S. M., & Gao, L. 2011, *MNRAS*, 415, 3177
 Rines, K., & Diaferio, A. 2006, *AJ*, 132, 1275
 Rozo, E., Nagai, D., Keeton, C., & Kravtsov, A. 2008, *ApJ*, 687, 22
 Schmidt, R. W., & Allen, S. W. 2007, *MNRAS*, 379, 209
 Shaw, L. D., Weller, J., Ostriker, J. P., & Bode, P. 2006, *ApJ*, 646, 815
 Springel, V. 2005, *MNRAS*, 364, 1105
 Springel, V., White, S. D. M., Jenkins, A., et al. 2005, *Natur*, 435, 629
 Sun, M., Voit, G. M., Donahue, M., et al. 2009, *ApJ*, 693, 1142
 Thomas, P. A., Muanwong, O., Pearce, F. R., et al. 2001, *MNRAS*, 324, 450
 Tormen, G., Bouchet, F. R., & White, S. D. M. 1997, *MNRAS*, 286, 865
 Vikhlinin, A., Burenin, R. A., Ebeling, H., et al. 2009, *ApJ*, 692, 1033

- Vikhlinin, A., Kravtsov, A., Forman, W., et al. 2006, [ApJ](#), **640**, 691
- Wechsler, R. H., Bullock, J. S., Primack, J. R., Kravtsov, A. V., & Dekel, A. 2002, [ApJ](#), **568**, 52
- Wechsler, R. H., Zentner, A. R., Bullock, J. S., Kravtsov, A. V., & Allgood, B. 2006, [ApJ](#), **652**, 71
- White, M. 2001, [A&A](#), **367**, 27
- White, M. 2004, [APh](#), **22**, 211
- White, M., Cohn, J. D., & Smit, R. 2010, [MNRAS](#), **408**, 1818
- Wojtak, R., & Lokas, E. L. 2010, [MNRAS](#), **408**, 2442
- Woodring, J., Heitmann, K., Ahrens, J., et al. 2011, [ApJS](#), **195**, 11
- Zappacosta, L., Buote, D. A., Gastaldello, F., et al. 2006, [ApJ](#), **650**, 777
- Zhan, H., & Knox, L. 2004, [ApJL](#), **616**, L75
- Zhao, D. H., Jing, Y. P., Mo, H. J., & Börner, G. 2003, [ApJL](#), **597**, L9
- Zhao, D. H., Jing, Y. P., Mo, H. J., & Börner, G. 2009, [ApJ](#), **707**, 354
- Zitrin, A., Broadhurst, T., Coe, D., et al. 2011, [ApJ](#), **742**, 117